Transitions in the vortex wake behind the plunging profile

Tomasz Kozłowski and Henryk Kudela

Department of Numerical Modelling of Flows, Wroclaw University of Technology, Wybrzeze Wyspianskiego 27, 50-370 Wroclaw, Poland

E-mail: tomasz.kozlowski@pwr.wroc.pl and henryk.kudela@pwr.wroc.pl

Communicated by Y Fukumoto

Abstract
In this study we investigate numerically the vortex wake formation behind the profile performing simple harmonic motion known in the literature as plunging. This research was inspired by the flapping motion which is appropriate for birds, insects and fishes. We assume the two dimensional model of flow. Depending on the parameters such as plunging amplitude, frequency and the Reynolds number, we demonstrate many different types of vortex street behind the profile. It is well known that the type of vortex wake determines the hydrodynamic forces acting on the profile. Dependences of the plunging amplitude, the Strouhal number and various topology vortices are established by constructing the phase transition diagram. The areas in the diagram related to the drag, thrust, and lift force generation are captured. We notice also the areas where the vorticity field is disordered. The disordered vorticity field does not allow maintenance of the periodic forces on the profile. An increase in the Reynolds number leads to the transition of the vortex wake behind the profile. The transition is caused by the phenomenon of boundary layer eruption. Further increase of the Reynolds number causes the vortex street related to the generation of the lift force to vanish.

(Some figures may appear in colour only in the online journal)

1. Introduction

Animals that fly and swim are devoid of rotating components, with their lift and thrust forces generated by a movement known as flapping. This flapping motion produces an instantaneous distribution of the velocity field around the profile, which leads to unsteady hydrodynamic effects. We refer to hydrodynamics, because most insects and birds fly in the regime of the

Mach number below $Ma < 0.2$. Therefore, the observed fluid phenomena can be treated as incompressible flow (Wang 2000). From the perspective of fluid mechanics, all fluid phenomena related to the generation of hydrodynamic forces are ruled by the dynamics of the vorticity field (Wu 1981, Wu et al 2005). The position of the vortices in the Karman vortex street leads to the defect of momentum and as a result generates a hydrodynamic drag force. It is known that the flapping profile causes a shift in the positioning of the vortices in the Karman vortex street and leads to an increase in fluid momentum and the generation of the thrust force (Jones et al 1996). This type of vortex street is called the reversed Karman vortex street.

The flapping system can be analysed in terms of Reynolds number Re Strouhal number St and dimensionless plunging amplitude A_C. When the kinematic parameters are properly selected, the vortex street can lose its symmetry and allow the lift force to be generated. If the vortex street is deflected upward, positive lift acting on the profile is created. It is believed that the direction of the vortex street inclination (up or down) is related to the direction of the initial flap (Godoy-Diana et al 2009).

A large number of different types of vortex street can be generally observed in the flapping motion (Lentink et al 2008, Schnipper et al 2009). They were collected in diagrams with the kinematic parameters of the flapping motion. On the basis of such characteristics, in Anderson et al (1998) it was shown that the highest efficiency of the flapping motion is obtained in the range of Strouhal number: $St = 0.2 \check{S} 0.4$. The experiment was performed at Reynolds number: Re 40 000. Observations of many bird species confirmed that they were flying in a range similar to the Strouhal number range (Taylor 2003). In Godoy-Diana et al (2008) it was shown that, in the discussed St range, generation of the lift and thrust force was accompanied by characteristic vortex wakes. This confirms the important role of fluid phenomena related to the reversal and deflection of the vortex street behind the flapping profile. In Jones et al (1996), it was shown experimentally that when $St > 1$, the direction of the vortex street deflection may change spontaneously. This means that within a certain range of flapping parameters, generating a positive lift may be difficult. Experimental observations have also been confirmed numerically for the two-dimensional flapping motion (Lewin and Haj-Hariri 2003).

In the present work, we studied numerically the formation of the vortex street and its transitions (to different types of vortex wake) behind the plunging profile. We observed the whole family of vortex streets, and created diagrams which linked the type of observed vorticity field using the Reynolds number function, the Strouhal number and the plunging amplitude. The main purpose of our simulations was to investigate the flow phenomena related to transitions of the vortex wake and how this transition depends on the Reynolds number. Increasing the Reynolds number intensified the formation dynamics of the vorticity field surrounding the profile. It was shown that the phenomenon known as 'boundary layer eruption', a sudden burst of the vorticity concentrated portion from the boundary layer into the main flow (Kudela and Malecha 2009b)—is possible. This phenomenon disturbed the formation of the vortex street and led to a disordered vortex field around the profile. It was also shown that the eruption phenomenon may lead to a change in the vortex wake s direction of deflection and cause a straightening of the vortex wake, and thus, a loss of lift at the flapping profile. For the numerical calculation we used the vortex-in-cell method (VIC). The importance of the VIC method lies in the possibility to analyse more directly the vorticity field since, in computations, particles that carry information about the vorticity field are used.

2. The vortex-in-cell method

2.1. Governing equations in a non-inertial reference-frame

The Navier–Stokes equation in primitive variables with coordinates fixed to a moving body takes the form (Wang 2004)

$$\frac{\partial \mathbf{v}}{\partial t} + \left(\mathbf{v} \cdot \nabla\right)\mathbf{v} = -\frac{1}{\rho}\nabla p + \nu\Delta\mathbf{v} - \frac{d\mathbf{V}_0}{dt} - \frac{d\Omega_0}{dt}\times \mathbf{r} - 2\Omega_0\times \mathbf{v} - \Omega_0\times \left(\Omega_0\times \mathbf{r}\right), \quad (1)$$

$$\nabla \cdot \mathbf{v} = 0, \quad (2)$$

where $\Omega_0 = (0, 0, \Omega_z)$ means the angular and $\mathbf{V}_0 = (V_x, V_y)$ the translation velocity vector of the profile, $r = (x, y)$ denotes the position vector, $\mathbf{v} = (v_x, v_y)$ is the velocity field and ν denotes the kinematic viscosity coefficient. We assumed a homogeneous flow with $\rho = 1$. The last three terms in equation (1) arise from a non-inertial coordinate system, and for the two dimensional space can be written as follows: the non-inertial force due to rotational acceleration $\frac{d\Omega_0}{dt} \times \mathbf{r} = (-\Omega_z y, \Omega_z x)$, the Coriolis force $2\Omega_0 \times \mathbf{v} = (-\Omega_z v_x, \Omega_z v_y)$ and the centrifugal force $\Omega_0 \times (\Omega_0 \times \mathbf{r}) = (\Omega_z^2 x, -\Omega_z^2 y)$. Taking the curl from both sides of equation (1), and introducing the stream function ψ, it can be transformed to the form (Gustafson et al 1991)

$$\frac{\partial\left(\omega + 2\Omega_z\right)}{\partial t} + \left(\nabla\omega\right)\cdot \mathbf{v} = \nu\Delta\omega, \quad (3)$$

$$\Delta\psi = -\omega, \quad (4)$$

$$v_x = \frac{\partial\psi}{\partial y}, \quad v_y = -\frac{\partial\psi}{\partial x}. \quad (5)$$

In two dimensional space the vorticity is given by the formula $\omega = \frac{\partial v_y}{\partial x} - \frac{\partial v_x}{\partial y}$ and it is related to the angular velocity Ω_z with equation $\omega = \nabla \times \mathbf{v} = 2\Omega_z$. Equations (3) and (4) represent a vorticity transport equation in a moving non-inertial reference frame for an observer moving with the body. The stream function far from a body due to translational velocity U_0, and the angular rotation $\Omega_z = \frac{d\alpha}{dt}$, can be written as

$$\psi_\infty = U_0\left(y\cos\left(\alpha\right) - x\sin\left(\alpha\right)\right) - \frac{\Omega_z}{2}\left(x^2 + y^2\right). \quad (6)$$

where α denotes the instantaneous angle between the chord of the profile and the velocity vector $\mathbf{V}_0$ and $U_0 = \sqrt{V_x^2 + V_y^2}$. The vorticity field in the laboratory frame differs only by a constant from the vorticity observed in the non-inertial frame (see equations (3) and (4)) therefore, we introduced the following change of variables

$$\omega^* = \omega + 2\Omega_z, \qquad \psi^* = \psi - \psi_\infty. \quad (7)$$

A detailed description of the solution to the Helmholtz equations in a moving reference frame can be found in Gustafson et al (1991).

2.2. The vortex-in-cell method for the conformal geometry

In the vortex-in-cell (VIC) method, the velocity field is obtained by solving Poisson equation (4) numerically on the grid. We use fast direct elliptic solver of fourth order. To better fit the grid to the solid boundary, we transformed the non-rectangular physical region (x, y) to one that was rectangular (ξ, η). On the figure we marked the suitable boundary conditions. The following conformal transformation was applied

$$x + iy = \cosh(\xi + i\eta). \tag{8}$$

In new variables (ξ, η), taking into account (7), equations (3) and (4) have the form

$$\frac{\partial \omega}{\partial t} + (\nabla \omega) \cdot \mathbf{u} = \frac{\nu}{J} \Delta \omega, \tag{9}$$

$$\Delta \Psi = -J\omega, \tag{10}$$

where J denotes a Jacobian of the conformal transformation

$$J = \det \begin{vmatrix} x_\xi & x_\eta \\ y_\xi & y_\eta \end{vmatrix}. \tag{11}$$

We have already omitted the star index. The velocity $\mathbf{u} = (u, v)$ in new variables is expressed by the formulas

$$u = \frac{1}{J} \frac{\partial \psi}{\partial \eta}, \qquad v = -\frac{1}{J} \frac{\partial \psi}{\partial \xi}. \tag{12}$$

Nullifying the normal velocity component is obtained by setting $\psi = $ const on the wall. The no-slip condition is realized by introducing a proper value of vorticity, that ensures the condition $\mathbf{u} \cdot \mathbf{s}^0 = 0$ where $\mathbf{s}^0$ denotes the tangential unit vector (Koumoutsakos et al 1994, Weinan and Liu 1996).

In the VIC method a continuous vorticity field is approximated by discrete particles distribution. The flow region is covered with the uniform numerical grid $h = \Delta\eta = \Delta\xi$. At every grid node, the particle with circulation $\Gamma_j = \int_A \omega \, d\xi d\eta$ is placed, where $A = h^2$ and

$$\omega(\xi, \eta) = \sum_p \Gamma_p \delta(\xi - \xi_p) \delta(\eta - \eta_p). \tag{13}$$

The viscous splitting (Cottet and Koumoutsakos 2000) algorithm was used to solve (9) and (10). Firstly, the inviscid fluid motion equation was solved

$$\frac{\partial \omega}{\partial t} + (\nabla \omega) \cdot \mathbf{u} = 0. \tag{14}$$

From (14) it stems that vorticity is constant along the trajectories of the fluid particles. According to Helmholtz theorems (Wu et al 2005), vortex particles moves like material fluid particles. Differential equation (14) may be replaced by a set of ordinary equations

$$\frac{d\xi}{dt} = u, \qquad \frac{d\eta}{dt} = v, \qquad \xi(0, \alpha_1) = \alpha_1, \qquad \eta(0, \alpha_2) = \alpha_2, \tag{15}$$

where $\alpha = (\alpha_1, \alpha_2)$ means the Lagrangian coordinate of fluid particles. The number of particles is equal to the number of grid nodes. Lagrangian parameter α takes in each time step the value $(\alpha_i, \alpha_j) = (\xi_i, \eta_j)$. The finite set of equations (15) was solved by the fourth order Runge–Kutta method. The velocity field was obtained by solving equation (10) on the numerical grid and utilizing (12). The particle velocities that were found between the grid

nodes were calculated by the interpolation formula

$$u\left(\xi_p, \eta_p\right) = \sum_j l_j\left(\xi_p, \eta_p\right) u_j, \tag{16}$$

where l_j denotes the two dimensional bilinear interpolation Lagrange base.

At the second step, in order to take viscosity into account a diffusion equation was solved

$$\frac{\partial \omega}{\partial t} = \frac{\nu}{J}\Delta\omega, \tag{17}$$

$$\omega\left(\xi, \eta, 0\right) = \omega_0, \quad \omega\big|_{wall} = \omega_s, \tag{18}$$

where ω_s was calculated on the basis of equation (10). The non-slip condition $u = 0$ was used for calculating the vorticity on the wall: $\omega_{(0,j)_s} = \check{S}\Psi_{\eta\eta}/J$. The value of $\Psi_{\eta\eta}$ was obtained from the Briley formula (Weinan and Liu 1996)

$$\omega_{(0,j)_s} = \frac{1}{J}\frac{108\Psi_{1,j} \check{S} 27\Psi_{2,j} + 4\Psi_{3,j}}{18\,h^2} + O\left(h^4\right), \tag{19}$$

where h denotes the grid step, index 0 refers to the wall and index i: $i = 1,2,3$ to the distance ih from the wall.

After particle displacement according to the ordinary differential equations (15), one has to transfer the vorticity from the particles to the grid nodes using an interpolation, see figure 2. It was done, according to the formula

$$\omega_{ij} = \frac{1}{h^2}\sum_p \Gamma_p \varphi_h(\xi)\varphi_h(\eta), \tag{20}$$

where

$$\varphi_h(\xi) = \varphi\left(\frac{\xi \check{S} \xi_i}{h}\right), \quad \varphi_h(\eta) = \varphi\left(\frac{\eta \check{S} \eta_j}{h}\right). \tag{21}$$

Indices p, i, j refer to the vortex particles and grid nodes respectively and $\varphi(\cdot)$ denote the kernels of the interpolation function. In the VIC method, the interpolation of particle masses onto the grid nodes is fundamental for the method's precision. In the present work the redistribution process was performed using Z-spline interpolation functions (Sagredo 2003). The main advantage of this approach was that high order symmetrical interpolation kernels could be simply constructed. The method also permitted us to obtain one-sided formulas, which we needed near the solid boundary. Fourth order Z-spline interpolation kernel Z_2 is identical with the known in literature $M4$ kernel and has the form (Sagredo 2003, Koumoutsakos and Leonard 1995)

$$\varphi(x) = \begin{cases} 1 \check{S} \frac{5}{2}x^2 + \frac{3}{2}|x|^3 & \text{for } |x| < 1 \\ \frac{1}{2}\left(2 \check{S} |x|\right)^2\left(1 \check{S} |x|\right) & \text{for } 1 \le |x| \le 2. \\ 0 & \text{for } |x| > 2 \end{cases} \tag{22}$$

To avoid losing mass of the vortex circulation, near the boundary we use one sided interpolation formula (Sagredo 2003). The one sided interpolation formula uses twelve nodes and the formula (22) uses sixteen nodes.

$$\varphi(x) = \begin{cases} 1 + \dfrac{1}{2}x^2 \check{S} \dfrac{3}{2}|x| & \text{for } j = 0, |x| \quad 1 \\[2mm] \check{S}\, x^2 + 2|x| & \text{for } j = 1, |x| \quad 1. \\[2mm] \dfrac{1}{2}x^2 \check{S} \dfrac{1}{2}|x| & \text{for } j = 2, |x| \quad 1 \end{cases} \tag{23}$$

Both interpolation kernels conserve the three first moments of the interpolated function.

$$\sum_{p} x_p^\alpha \varphi\left(\frac{x_p \check{S} x}{h}\right) = x^\alpha, \qquad \alpha = 0, 1, 2. \tag{24}$$

After redistribution, the diffusion equation (17) was solved. We used the grid-based alternating direction implicit (ADI) scheme (Thomas 1995)

$$\omega^{n+\frac{1}{2}} = \omega^n + \frac{\Delta t}{2J}\nu\left(\Lambda_{\xi\xi}\omega^n + \Lambda_{\eta\eta}\omega^{n+\frac{1}{2}}\right), \tag{25}$$

$$\omega^{n+1} = \omega^{n+\frac{1}{2}} + \frac{\Delta t}{2J}\nu\left(\Lambda_{\xi\xi}\omega^{n+1} + \Lambda_{\eta\eta}\omega^{n+\frac{1}{2}}\right), \tag{26}$$

where Λ means the three point central finite difference quotient with respect to the variable that was put in the lower index. Solving the diffusion equation ended our calculations in the nth time step of the VIC method. The VIC method was very carefully tested and results were published in several of our papers (Kudela and Malecha 2009a, Kudela and Kozlowski 2009).

2.3. Unbounded domain

In the VIC method we used the numerical grid, therefore the computation domain had to be finite. To establish the boundary condition for the stream function far from the body we used the method described in Anderson and Reider (1996) and Wang (1999). The method takes advantage of the fact that the non zero vorticity domain is limited to the finite domain surrounding the solid body immersed in the fluid. At a far distance from the body where the vorticity equals zero, the asymptotic properties of the solution of the Laplace equation and its representation by Fourier series was used. A detailed description for obtaining the correct boundary value applied in our present work can be found in Kudela and Kozlowski (2009) and Wang (1999).

2.4. Hydrodynamic forces

The hydrodynamic forces acting on the wing were calculated using the vorticity distribution on the surface of the ellipse. Expressing the fluid forces by the pressure force $\mathbf{F}_p$ and the viscous force $\mathbf{F}_\nu$, one can obtain

$$\mathbf{F}_p = \nu\rho b \int_C \frac{\omega}{\mathbf{n}}dC + \rho b A_b \frac{d\mathbf{U}_0}{dt}, \tag{27}$$

$$\mathbf{F}_\nu = \nu\rho b \int_C \omega \mathbf{s}^0 dC, \tag{28}$$

where b denotes the unit contractual length, ρ density of the fluid, $\mathbf{n}$ and $\mathbf{s}^0$ are normal and tangential unit vector respectively and A_b is the area of the body. The last term on the right side in equation (27) represents the inertial force of the fluid displaced by the profile (Sane 2003). The forces obtained from equations (27) and (28) were decomposed into
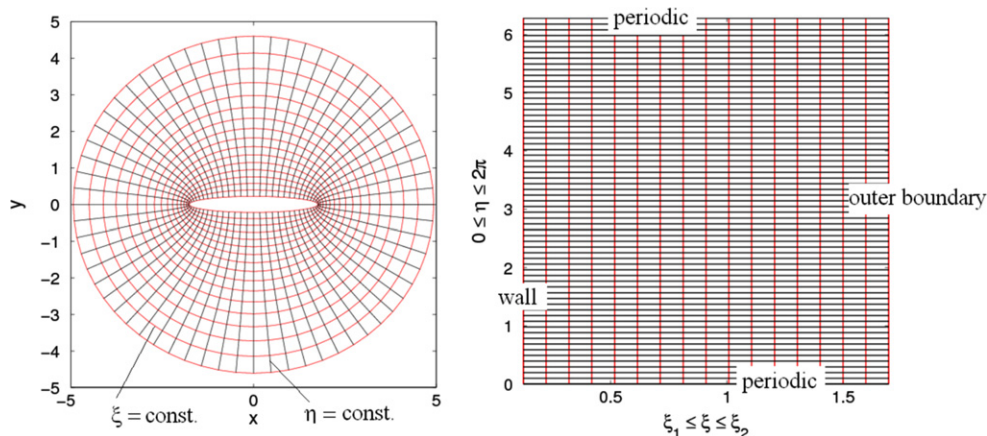
Figure 1. Elliptical grid in the physical domain.

horizontal F_D and vertical F_L components, which in turn correspond to the drag and lift forces. The force coefficients were calculated according to relations

$$C_D = F_D \Big/ \frac{\rho}{2} U_0^2 cb, \qquad C_L = F_L \Big/ \frac{\rho}{2} U_0^2 cb, \tag{29}$$

where U_0 denote the free stream translational velocity.

3. Simulation of flow around the plunging profile

3.1. Formulation of the problem and computational details

In our study we used the elliptic profile with the given equation (Shyy et al 2008)

$$y(t) = \frac{A_0}{2} \cos\left(2\pi ft\right), \tag{30}$$

where $y(t)$ denotes the instantaneous position of the profile center, A_0 is the amplitude and f is the frequency of the plunging. The profile s vertical velocity was calculated from the formula $v = \frac{dy}{dt}$. Far from the body, we assumed that velocity of the fluid U_0 is constant, see figure 3.

   The flow over the plunging body can be characterized by the following set of non-dimensional parameters: Reynolds number Re, Strouhal number St and plunging amplitude A_C (Godoy-Diana et al 2008, Shyy et al 2008):

$$Re = \frac{U_0 c}{\nu}, \quad St = \frac{fc}{U_0}, \quad A_C = \frac{A_0}{c}, \quad St_A = \frac{A_0 f}{U_0}, \tag{31}$$

where c is the profile chord of the profile and ν denotes the kinematic coefficient of fluid viscosity. Following Godoy-Diana et al (2009) and Shyy et al (2008), we introduced two definitions of the Strouhal number. The Strouhal number denoted with (St) is sometimes referred to as reduced frequency.

   The profile chord was set to c = 2 and thickness of the profile $e = \frac{b}{c} = 0.2$. We performed the calculations for the Reynolds number Re = 100, Re = 250 and Re = 500 with homogeneous fluid $\rho = 1$. The plunging frequency was fixed to f = 0.5 and the Strouhal number (St) was controlled by changing the free stream velocity U_0. Calculations were carried out for
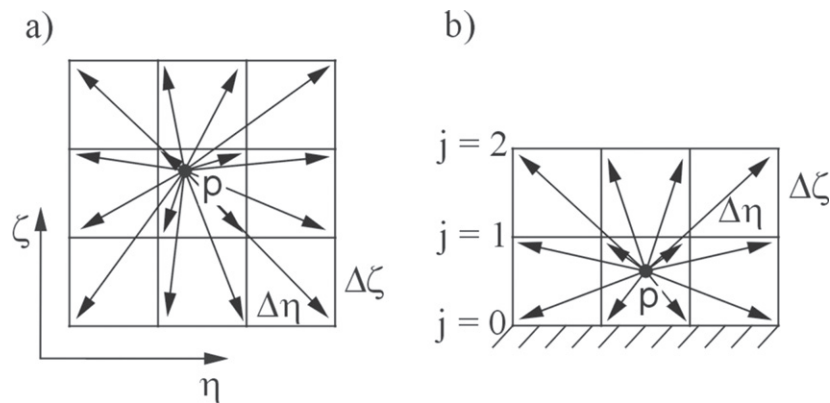
Figure 2. Redistribution of the particle masses onto the neighboring grid nodes, (a) for particles laying inside the computational domain (at least one cell from the wall), (b) for particles in the vicinity of the wall.

dimensionless time $T = ft$, in the range $T = (0, 10)$ which corresponds to ten periods in equation (30).

We used the elliptical mesh shown in figure 1, with 256 grid nodes in a radial direction and 256 grid nodes in an azimuthal direction: (ξ, η), $\xi = (\xi_1, \xi_1 + 2\pi)$, $\xi_1 = 0.2$ and $\eta = (0, 2\pi)$. For each time step, we corrected the boundary condition for the stream function far from the body, as detailed in a previous section.

3.2. Vortex wakes behind the flapping profile, Re = 100

In figures 4–8 various vortex wakes behind the flapping profile are presented. On the left side of the figures, the vortex street was visualized by passive particles that were taken by fluid from the close vicinity (the particles were placed around the profile s perimeter in two layers: as numerical grid steps one and two) of the solid boundary. On the figures, right sides, vorticity and streamlines are presented.

For Reynolds number $Re = 100$ and small plunging amplitudes we observed stationary vortex bubbles behind the foil. When the amplitude was increased, the vortex bubbles were no longer stationary. They formed the Karman vortex street behind the body shown in figure 4. By Karman vortex street we understand that the vorticity field where the vortices are shed from the upper (lower) side of the profile stays on the upper (lower) side of the axis of profile s symmetry. The position of vortices in the wake reduces the fluid momentum and causes drag generation. Loss in the fluid momentum can be simply interpreted from the time averaged velocity profile in the vortex wake denoted in the figures with black arrows.

The situation presented in figure 5 ($St = 0.8$, $A_C = 0.5$) is called aligned vortices (av). It means that the vortices in the wake are placed on the axis of the profile s symmetry. When the amplitude was further increased, the vortices switched their position. The vortices that were created on the upper side of the profile changed their position in the wake and moved to the lower side of the axis of the profile s symmetry, see figure 6. The counter-rotating vortices in the wake increased the fluid momentum causing the thrust force generation. That vortex street is called the reversed Karman vortex street (Jones et al 1996). In such a configuration, the thrust force is produced $C_D < 0$. For the reversed vortex street, one can find such plunging parameters that will cause the drag force to equal zero.
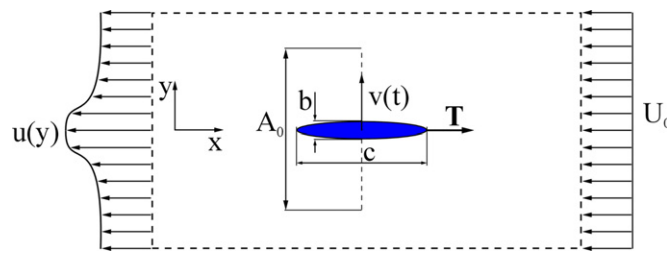
Figure 3. Scheme of the plunging airfoil immersed in the fluid.

Further increase of the plunging amplitude and the Strouhal number ($St = 0.8$, $A_C = 1.0$) led to the wake s asymmetry and deflection of the reversed Karman vortex street from its horizontal direction, see figure 7. This phenomenon is responsible for lift force generation (Jones et al 1996, Platzer and Jones 2000). The wake deflection s direction depends on the first flap (up or down) and determines the lift force sign (positive or negative). Although the discussed phenomenon was first observed in the 1950s, we are still waiting for a full explanation (Godoy-Diana et al 2009). Higher amplitude and the Strouhal number resulted in a loss in vortices arrangement and a disordered vorticity field generation (see figure 8). The disordered vorticity field caused random hydrodynamic forces to act on the profile.

One can summarize the above results in a phase transition diagram. In figure 9 we show the relation between the vortex wake type and the plunging parameters: the Strouhal number St and amplitude A_C. The drag (C_D) and lift (C_L) coefficients are also depicted.

Generating thrust force for the reversed Karman vortex street appeared only over the $C_D = 0$ curve. Positive lift force appeared over the $C_L = 0$ curve and was present in the deflected reversed Karman vortex street s whole region.

A similar phase space diagram for (St, A_C) was obtained experimentally by pitching the profile (Godoy-Diana et al 2008, 2009). The experimental data shown in the cited papers relate to the foil that is subjected to motion with variable angles of attack, known in the literature as pitching. In the numerical results, the foil performed only the plunging motion, as depicted in figure 3. The Reynolds number defined with respect to the wing chord was different (we assumed $Re = 100$ and in the cited work $Re = 1173$). The qualitative agreement of the our calculations with the discussed experimental data may suggest that in the given Reynolds number regime, thrust and lift force generation mechanisms are comparable.

3.3. Influence of the Reynolds number

Based on the numerical calculations, we constructed phase transition diagrams for Reynolds numbers $Re = 250$ and $Re = 500$. In this range of the Reynolds number we observed another type of vortex wake—the **2P** vortex wake, recognized for its flow around an oscillating cylinder (Ponta and Aref 2006) and also for the flapping foil as noticed in Schnipper et al (2009). Symbol **2P** means that during a single foil motion (up or down) two vortex structures each with two vortices with opposite circulation were created, see figure 10. From the experiment it is known that this type of vortex wake may be important in fish locomotion (Müller et al 2008). The phase diagrams for the Reynolds number $Re = 250$ and $Re = 500$ are presented in figures 11(a) and (b). We observed that if the Reynolds number increased, the region with reversed and deflected vortex wake (denoted with ■) vanish and for the Reynolds number $Re = 500$ disappeared completely. For the Reynolds number $Re = 500$ the transition process proceeded from the reversed Karman vortex street directly to the chaotic vorticity
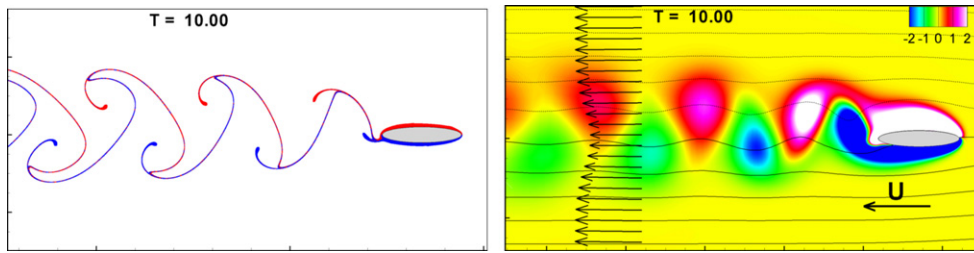
Figure 4. Karman vortex street generated by flapping motion of the profile, with St = 0.6 and A_c = 0.25. On the left visualisation by passive markers is presented, on the right the vorticity field with streamlines. The arrows behind the profile denote the averaged velocity field. This kind of vortex street was marked with ⋆ in figure 9.
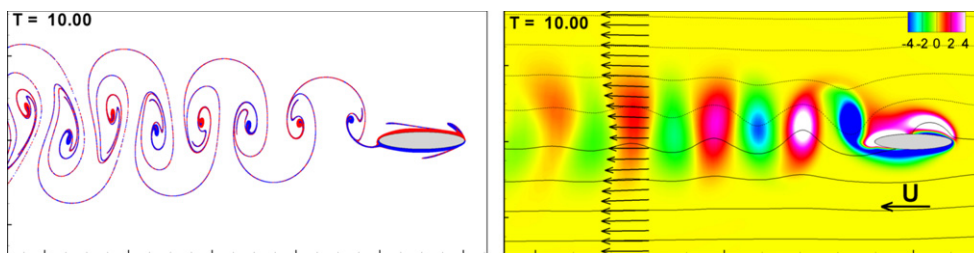

Figure 5. Aligned vortices generated by plunging motion with St = 0.8 and A_c = 0.5. The vortex wake corresponds to the transient region, in figure 9, denoted with ▲.
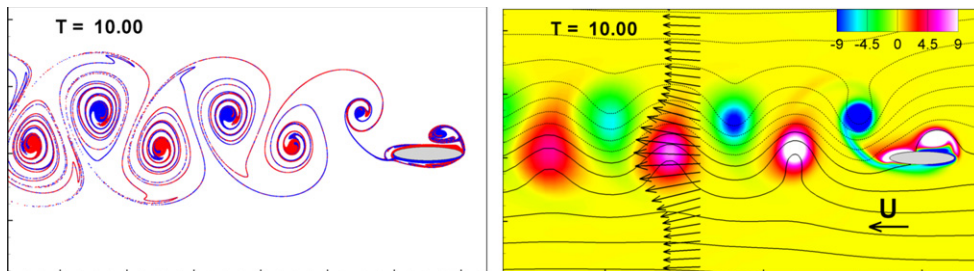
Figure 6. Thrust generation by the plunging profile with St = 0.8 and A_c = 0.75. The reversed Karman vortex street is denoted with ● in figure 9.

field (see figure 11(b)). It means that in this range of parameters the generation of the vertical force connected with the deflection of the vortex wake is not possible.

We performed additional calculations near the transition line (this line separates the reversed Karman vortex street from the disordered vorticity field, see figure 11) and we did not observe any deflection of the vortex wake after ten periods of motion. Unexpectedly, however, the deflection sometimes existed at the beginning of the flapping motion, but after a few foil periods the vortex wake became straight, see figure 12. In the investigated range of parameters, the hydrodynamic effects were dominated by the phenomenon of a sudden separation and eruption of the boundary layer from the profile. By the eruption of the boundary layer we mean the ejection of the fluid portion near the wall to the external flow
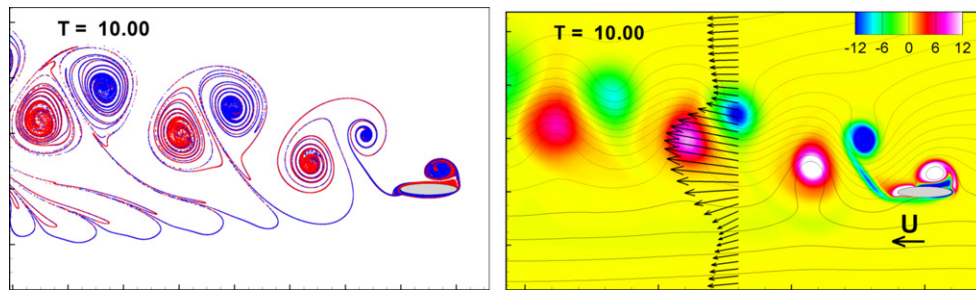
Figure 7. Deflected vortex wake behind the plunging profile with St= 0.8 and A_c = 1.0. The upward deflection of the wake results in lift generation, denoted in figure 9 with ■.
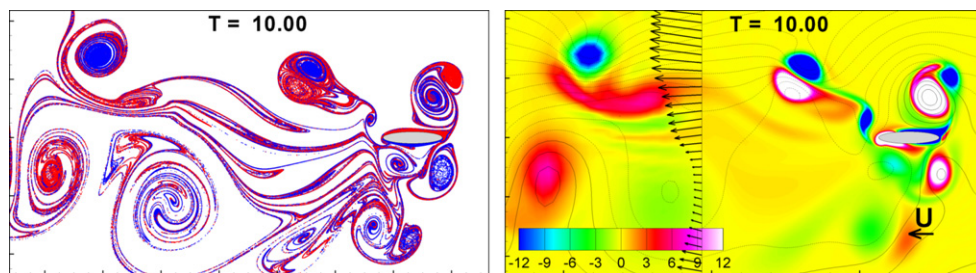

Figure 8. Random vorticity field generated by plunging foil with high value of Strouhal number St= 1.2 and amplitude A_c = 1.0. The presented case corresponds to the region denoted with ◆ in figure 9.

area. This ejection is caused by the vortex patch, which is created above the wall. One can notice that in the flow over profile the leading edge vortex is created in every period of motion, see figures 4–8. If the intensity of the produced leading edge vortex was sufficiently high, it induced the vortex with opposite circulation on the wall, see figure 13, frame T = 6.55. The leading vortex and induced vortex with opposite circulation form dipolar vortex structure which carry the fluid from the wall to external flow area, 13, frame T = 7.20. The dynamics of the boundary layer eruption increase with the Reynolds number. A detailed description of the discussed phenomenon can be found in Kudela and Malecha (2009b) and Doligalski et al (1994). The eruption phenomena led to the loss of the vortex wake deflection and caused the vortex wake type to change. It seems that the reason for the loss of deflection is in nonlinear inertial terms in the fluid motion equations whose importance increased when the viscosity was lowered. Straightening of the vortex wake and vanishing of the deflected wake region by increasing the Reynolds number requires further experimental investigation.

By observing natural flyers, it was found that they operated with the Strouhal number (equation (31), fourth formula) regime of St_A = 0.2Š 0.5 (Taylor 2003). The experimental work of Anderson et al (1998) demonstrated that the highest flapping efficiency occurs in the Strouhal number regime: St_A = 0.2Š 0.4. Experimental results are consistent with the observations of flying birds and insects (Anderson et al 1998). It is worth noting that in using the von Karman analysis for vortex street stability behind the cylinder, the Strouhal number for the stable vortices configuration equals St_A = 0.26 (Kochin et al 1964). In figures 9 and 11 the curves of constant Strouhal number St_A were shown. For the simple two dimensional plunging
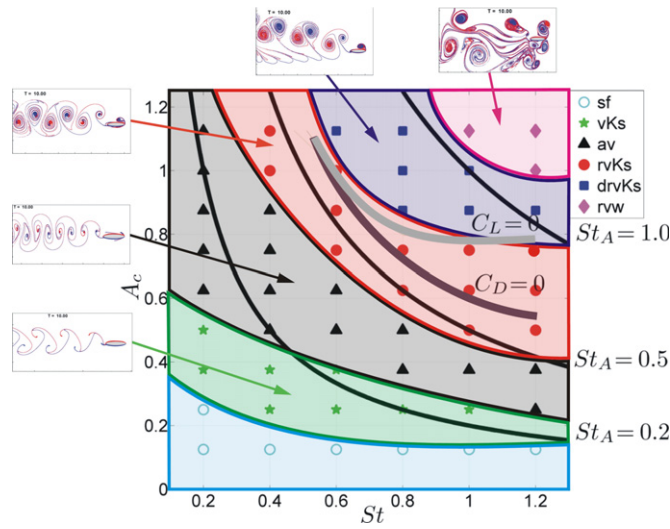
Figure 9. Relationship between Strouhal number St, nondimensional flapping amplitude A_c and vortex topology in the wing wake, for the Reynolds number $Re = 100$. Symbols denote: $\bigcirc$—steady flow, $\star$—Karman vortex street, $\blacktriangle$—aligned vortices, $\bullet$—reversed Karman vortex street, $\blacksquare$—deflected reversed Karman vortex street, $\blacklozenge$—chaotic vortex wake.
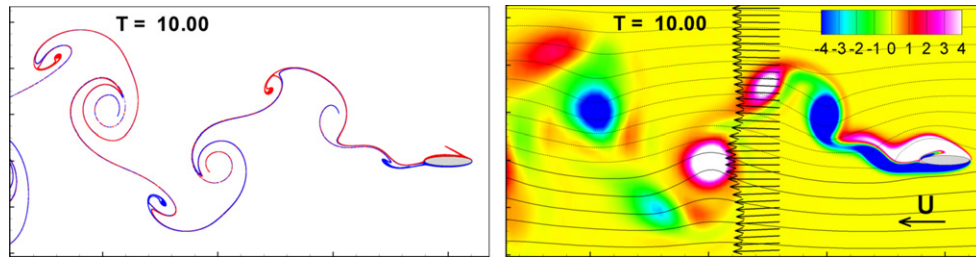

Figure 10. 2P vortex wake, generated by plunging foil with Strouhal number $St = 0.2$, amplitude $A_C = 1.0$ and Reynolds number $Re = 250$. This case corresponds to the region denoted with $\blacktriangledown$ in figure 11.

motion investigated in the present paper, the Strouhal number range related to the lift and thrust force generation depended on the Reynolds number. For $Re = 100$, the vortex wakes generating the thrust and lift forces are within the range $St_A = 0.6\check{S} 1.1$, which is similar to the results presented for the freely plunging profile (Schnipper et al 2009). With increased Reynolds number, the zone of the thrust force generation moves in the transition diagram and for the Reynolds number $Re = 500$ it contains the region with the optimal flapping Strouhal number (St_A) observed in nature.

Conclusions

In the paper the VIC method was used to investigate hydrodynamic phenomena appropriate for the flapping motion. Due to the large number of effects relating to unsteady
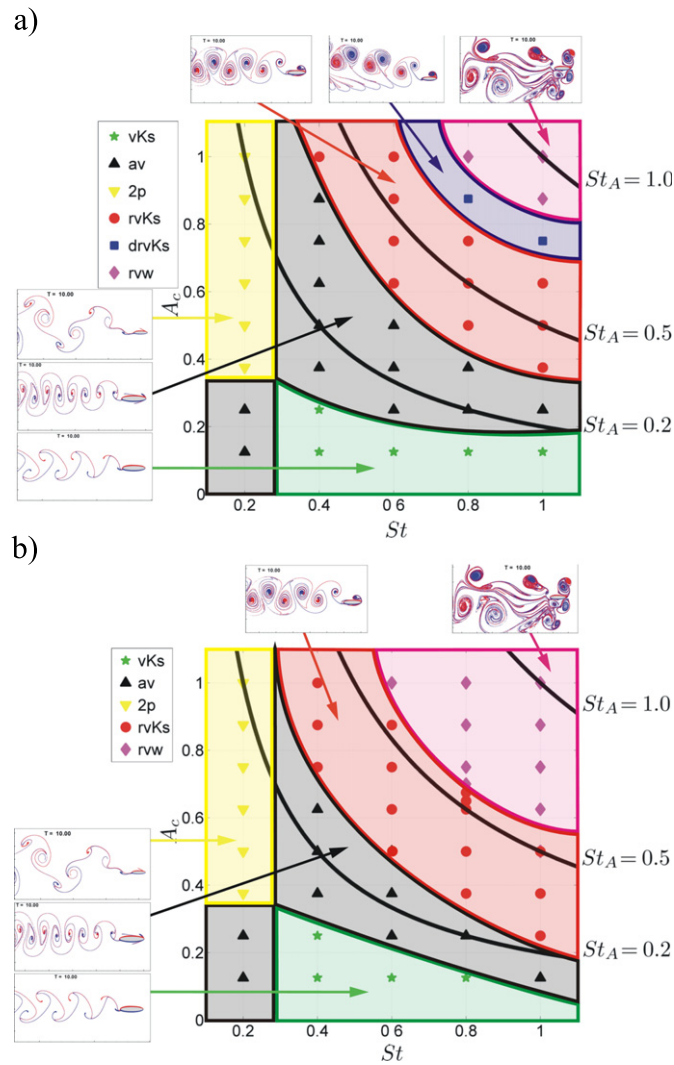
Figure 11. Relationship between Strouhal number St, nondimensional flapping amplitude A_c and vortex topology in the wing wake, (a) $Re = 250$ and (b) $Re = 500$. Symbols in the figure denote: ▼—**2P** vortex wake, *—Karman vortex street, ▲—aligned vortices, ●—reversed Karman vortex street, ■—deflected reversed Karman vortex street, ♦—chaotic vortex wake.

hydrodynamics and the large number of flapping parameters, we decided to use a two-dimensional flow model. This made it possible to focus on the fundamental fluid phenomena responsible for creating the lift and the thrust force in the flapping motion. Despite the two-dimensional simplification, the fluid dynamics is very rich and permits one to understand the nonlinear nature of the flapping effects on the vorticity flow structure. For any given plunging motion of the profile we observed a whole family of different types of vortex wakes. We built transition diagrams parameterized with the Strouhal number and dimensionless plunging amplitude. We presented how the vortex wake changed with the Reynolds number. For large Reynolds number we observed the vortex wake type transition and the loss of vortex
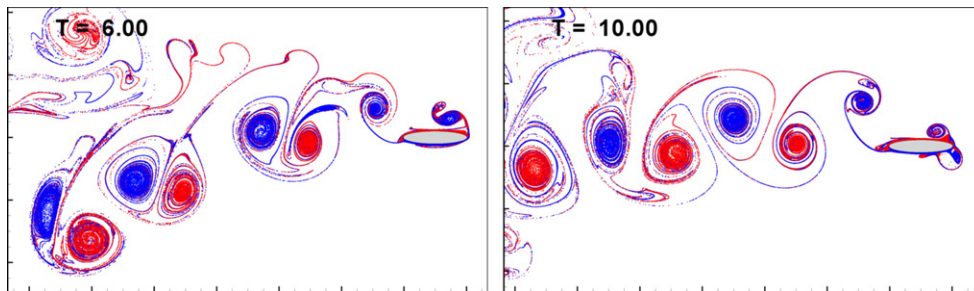
Figure 12. Effect of straightening the vortex wake caused by the dynamic eruption of the boundary layer, $St = 0.8$, $A_C = 0.675$, $Re = 500$.
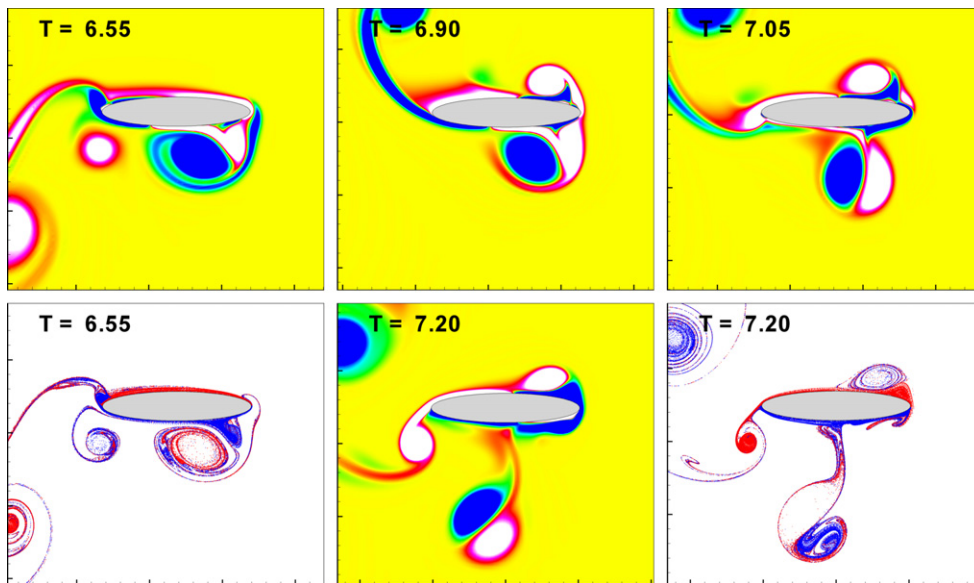

Figure 13. The boundary eruption phenomenon on the flapping area of the profile, $Re = 500$, $St = 0.8$, $A_C = 0.675$. In the figure the vortex field is presented for nondimensional time $T = 6.55\check{S}\,7.20$. The visualization with passive markers is also presented.

deflection. For large Reynolds number we observed the vortex wake type transition and the loss of vortex deflection. The loss of vortex deflection is caused by the sudden eruption of the boundary layer on the profile. This eruption disturbed the formation of the vortex street. Increasing the Reynolds number intensified the eruption of boundary layer that causes the disordered vorticity field around the profile. An increase in the Reynolds number extends the zone of parameters for which we observed the disordered vorticity field and in the profile s disordered distribution of hydrodynamic forces. The computational results are in qualitative agreement with the experimental data presented in Godoy-Diana et al (2008) and Lentink et al (2008) although we had assumed a much smaller Reynolds number and the basic plunging motion of the profile. As one can notice by the inspection of the diagrams in figures 9 and 11, the parameters of plunging motion should keep in suitable limits in order to